JACS Au
AN OPEN ACCESS JOURNAL OF THE AMERICAN CHEMICAL SOCIETY

pubs.acs.org/jacsau
Article

Visualizing Reactive Oxygen Species-Induced DNA Damage Process in Higher-Ordered Origami Nanostructures

Shuangye Zhang,[§] Xiaodong Xie,[§] Hairuo Zhang, Ziwei Zhao, Kai Xia, Haitao Song, Qian Li, Mingqiang Li,* and Zhilei Ge*

Cite This: *JACS Au* 2025, 5, 965−974
Read Online

ACCESS | Metrics & More | Article Recommendations | Supporting Information

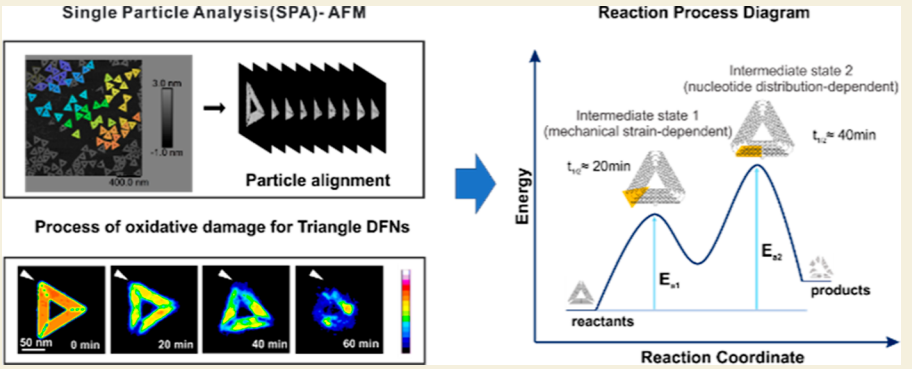

ABSTRACT: The genetic information on organisms is stored in the cell nucleus in the form of higher-ordered DNA structures. Here, we use DNA framework nanostructures (DFNs) to simulate the compaction and stacking density of nucleosome DNA for precise conformational and structure determination, particularly the dynamic structural changes, preferential reaction regions, and sites of DFNs during the reactive oxygen species (ROS) reaction process. By developing an atomic force microscopy-based single-particle analysis (SPA) data reconstruction method to collect and reanalyze imaging information, we demonstrate that the geometric morphology of DFNs constrains their reaction kinetics with ROS, where local mechanical stress and regional base distribution are two key factors affecting their kinetics. Furthermore, we plot the reaction process diagram for ROS and DFNs, showing the reaction process and intermediate products with individual activation energies. This SPA method offers new research tools and insights for studying the dynamic changes of highly folded and organized DNA structural domains within the nucleus and helps to reveal the key mechanisms behind their functional differences in topologically associating domains.

KEYWORDS: *reactive oxygen species, DNA damage process, DNA framework nanostructures, single particle analysis, AFM imaging*

INTRODUCTION

The essential information on organisms to sustain life is stored within cells in the form of higher-ordered DNA structures.[1,2] However, the damage for these DNA structures from reactive oxygen species (ROS)[3] could destabilize the chromatin's topological structure and the genome's integrity,[4,5] resulting in the loss of genetic information, ultimately impairing the survival capability of the living organisms.[6−8] Meanwhile, due to the tight arrangement and high concentration of DNA within cell chromosomes,[9−11] intracellular studies are greatly limited. Hence, it is highly challenging to establish an extracellular model and visualize their dynamic processes during ROS damage.

DNA nanotechnology utilizes the principle of complementary base pairing of DNA, facilitating higher-ordered stacking assembly of DNA double strands through the design of DNA folding pathways, and constructs DNA higher-ordered assembly structures with different topological morphologies and stacking densities, displaying different physical, chemical, and mechanical character.[12−15] This unique ability has been widely used in research on biomimetics and nanomanufacturing.[16−28]

Here, we have constructed a series of DNA framework nanostructures (DFNs) with different topologies to simulate the structural characteristics of the higher-ordered DNA structures packaged in cell chromosome and developed an AFM-based single-particle analysis (SPA) method[29] to locate and monitor the kinetic process of DNA damage induced by ROS in real-time, facilitating the investigation of both global and localized damage. We found that topological differences of DFNs underlie

Received: December 10, 2024
Revised: January 13, 2025
Accepted: January 15, 2025
Published: January 23, 2025

https://doi.org/10.1021/jacsau.4c01203
JACS Au 2025, 5, 965−974

the reaction kinetics of the ROS damage reaction. Subsequently, we identified that the mechanical stress and base distribution within DNA structures are two principal factors influencing the reaction rate. Regions with high mechanical stress and abundant G bases are more prone to being damaged, which is caused by the vulnerability of topological stress and the reactivity of the bases. In the simulated ROS damage reaction process, we found that the activation energy-dependent on mechanical stress is lower than that dependent on base distribution, which generated a faster reaction rate. These findings provide new research tools and insights for studying ROS damage in highly folded and stacked DNA structural domains within the cell nucleus.[30,31]

RESULTS AND DISCUSSION

SPA of Higher-Ordered DNA Structures during ROS Damage

A DNA nucleosome is the basic unit of DNA packaging in eukaryotic cells, where the DNA could be packaged into condensed, compact, and higher-ordered structures. The high DNA packaging density allows DNA to be effectively stored in a compact manner within the nucleus, protecting the DNA molecules from ROS damage and maintaining the stability and functionality of chromosomes.[2,32,33] To better simulate the structural characteristics of the nucleosome, we thus artificially constructed DFNs mimicking their folding and compaction in extracellular environments (Figures 1a and S1−S4).

Since DNA damage is induced by ROS, including base damage loss and DNA strand breakage, which could fragment the integrity of DNFs, their overall surface coverage on mica during AFM scanning can be monitored accordingly, which means that the overall structural dynamics of DFNs can be tracked by collecting images by AFM before and after the reaction. Here, we employed graphitic carbon nitride (g-C_3N_4) nanomaterial as a photosensitizer to generate hydroxyl radicals ($^{\bullet}$OH) to study their oxidative damage reactions with DFNs of different topologies. First, g-C_3N_4 and catalase (hydrogen peroxide scavenger) were mixed to generate $^{\bullet}$OH individually. After a 60 min reaction, the structural damage of DFNs caused by $^{\bullet}$OH can be observed through AFM (Figure 1b).

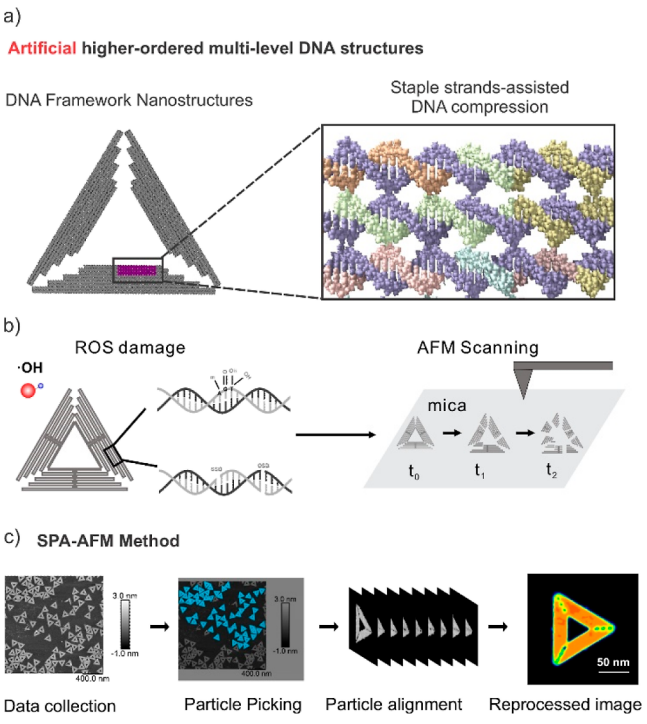

Figure 1. SPA of higher-ordered DNA structures during ROS damage. (a) Construction of artificial higher-ordered DNA structures. (b) Experimental process of ROS-induced DNA damage. (c) Workflow of SPA-AFM.

Further quantitative analysis of the average area of DFNs can demonstrate the process and degree of reactions with different reactants. However, this statistical data processing model can yield only an overall reaction efficiency and lacks the ability to differentiate the reaction sites and regions of individual DFNs. Therefore, we introduced SPA into AFM data processing,[29,32,33] which includes a large number of single-particle image collections, coarse annotation, fine contour searching, and particle alignment to obtain structural and conformational changes in DNA assemblies after reaction with ROS (Figure 1c). This SPA-AFM data reprocessing method has provided additional reaction information, such as the dynamic and preferential reaction regions of DNA damage caused by ROS, which holds great potential for further investigation of the structure and function of DNA structural domains during time-dependent monitoring.

Therefore, in order to better simulate the structural characteristics of higher-order DNA structures (Figure 1a), we thus artificially designed a series of DFNs based on the compaction and stacking density of DNA helical bundles. By adjusting the folding pathway of DNA,[34−36] we have assembled four DNFs, including rectangle, triangle, cross, and regular hexagon-shaped nanostructures mimicking their folding and compaction in extracellular environments (Figure 1b).

Geometric Morphology of DFN Constrains Their Reaction Kinetics of ROS Damage

We first tested the reactivity of triangle DFNs with $^{\bullet}$OH by monitoring the AFM images at different time points during the reaction (Figure S5). The AFM results showed that ROS could effectively deformed the structure of DFN, and the structural damage extent could directly reflect the reaction process.

We further conducted the SPA data processing procedure based on multiple AFM images and found the preferential damage regions in triangle DFNs. The damage localization results showed that the damage reactions happened in vertices first and then went to edges during the first 60 min. Hence, we anticipated that the kinetics of $^{\bullet}$OH-induced DFN damage had a geometric-dependent manner.

Since the dynamics of many natural systems are fundamentally constrained by their underlying structures,[37,38] we hence examine the degree to which geometric morphology can determine diverse kinetics of ROS damage. Therefore, we have designed and built a series of artificial DFNs in different configurations to increase the morphological diversity, including rectangle, triangle, cross, and regular hexagon-shaped DFNs (Figure 2a).

Subsequently, we conducted experiments on various DFNs to study ROS damage and collected 50 single-particle AFM images (Figures S6−S9). After SPA processing, we were able to observe the dynamic changes and damaged regions of high-order DNA structures with different topologies during ROS damage. In Figure 2b, we observed that triangle-shaped DFNs exhibited noticeable damage after 20 min, disintegrating by 60 min, whereas hexagon-shaped DFNs started to show significant damage at 40 min but retained their structural shape at 60 min.

https://doi.org/10.1021/jacsau.4c01203
JACS Au 2025, 5, 965−974

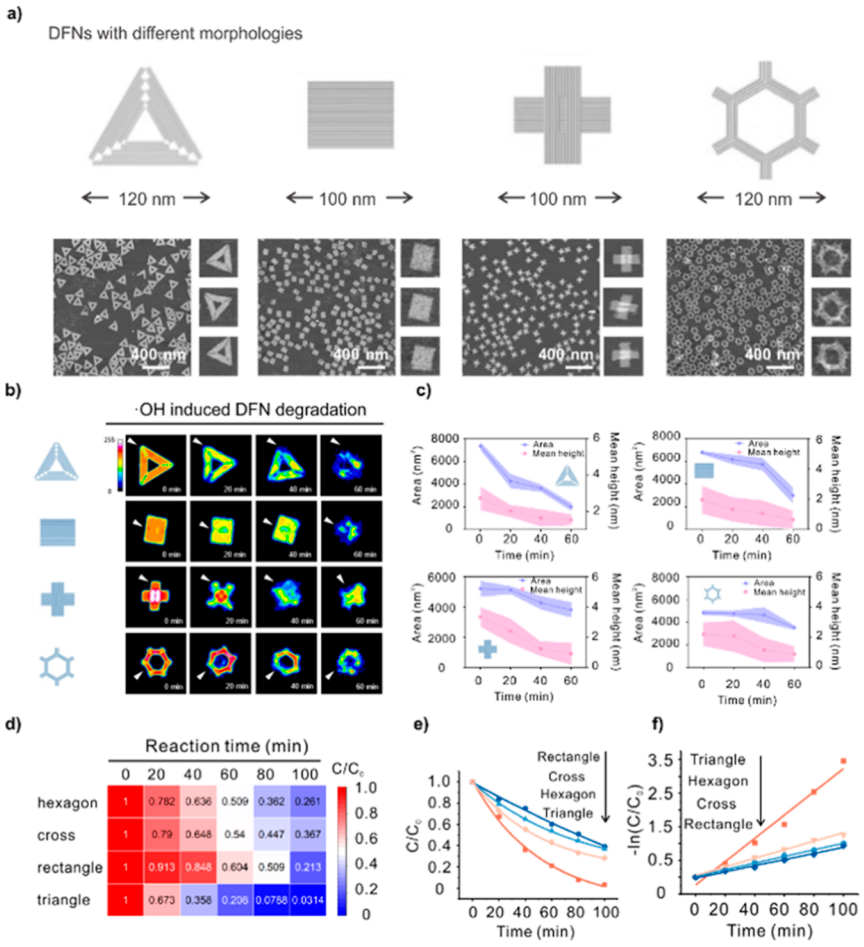

Figure 2. Geometric morphology of DFN constrains their reaction kinetics of ROS damage. (a) Construction of rectangle, triangle, cross, and regular hexagon-shaped DFNs. (b) SPA processing of •OH-induced structure deformation in time-dependent manner. (c) Analysis of the total area and height changes in the SPA images of the reaction between DFNs and ROS. (d) Heat map showing the time-dependent changes in the average area of each DFN with different topological properties. (e,f) Kinetic curves of the reaction, first-order reaction kinetics equations between DFNs with •OH.

Meanwhile, with the help of SPA, we found that the preferential damage reaction sites of four DFN structures were different: for triangular DFNs, the majority of the structural damage gathered at the vertices of the triangle in the beginning; for rectangular DFNs, they appeared at the center of rectangles first; and for cross- and honeycomb-shaped DFNs, they prefer reacting along the linear edges.

Next, in order to investigate the influence of the topological structure of DFNs on the oxidative damage reaction process to obtain more comprehensive information about DNA oxidative damage, we systematically examined the reaction kinetics between DFNs and •OH. Quantitative results were based on the average relative area of the DFNs' differences in their degrees of deformation at different time points. We then conducted further statistics on the retained area and structural height of each DNA higher-ordered structure (Figures 2c and S14), and based on their area dynamic, we further plotted heat maps for each structure, which illustrated the differences in reactivity among DFNs with different topologies (Figure 2d), and the kinetic curves of different structures' reactions with •OH (Figure 2e,f). The fitted curve demonstrated that all the reactions followed the first-order reaction kinetics equation ($\ln(C/C_0) = kt$), and the apparent rate constants for triangle, hexagon, cross and rectangle-shaped structure were 34.7×10^{-3}, 13.21×10^{-3}, 9.9×10^{-3}, and 9.2×10^{-3} min^{-1}, respectively, where triangle-shaped DFNs exhibited the fastest reaction with ROS. After calculating the half-time of each reaction, we found the half-time for triangle, hexagon, cross, and rectangle structures were 20.0, 52.5, 70.2, and 75.6 min, respectively, where triangle-shaped DFNs exhibited the shortest half-time with ROS (Figure S9). Agarose gel also exhibits differences in the dynamics of various topological structure DFNs (Figures S10−S13).

Given that the designed higher-ordered DFNs utilized the same DNA scaffold strand with identical sequences, the variations in their reaction kinetics should lie in the differences of their topological structures. First, different folding directions of DNA strands in DFNs make DNA at specific regions (corners) more exposed, and the reduced spatial steric hindrance at specific locations make those DNA more susceptible to be attacked; second, compared to inner edge areas, outer edge areas are prone to being damaged due to the lower stacking density. Therefore, we believe that the sensitivity of DNA higher-order structures to ROS reactions strongly depends on their geometric morphology.

Mechanical Stress-Dependent ROS Damage for Higher-Ordered DFNs

In order to better explore the heterogeneity of oxidative damage in DNA topological structures and its key mechanism, we conducted further SPA studies using highly reactive triangular

https://doi.org/10.1021/jacsau.4c01203
JACS Au 2025, 5, 965−974

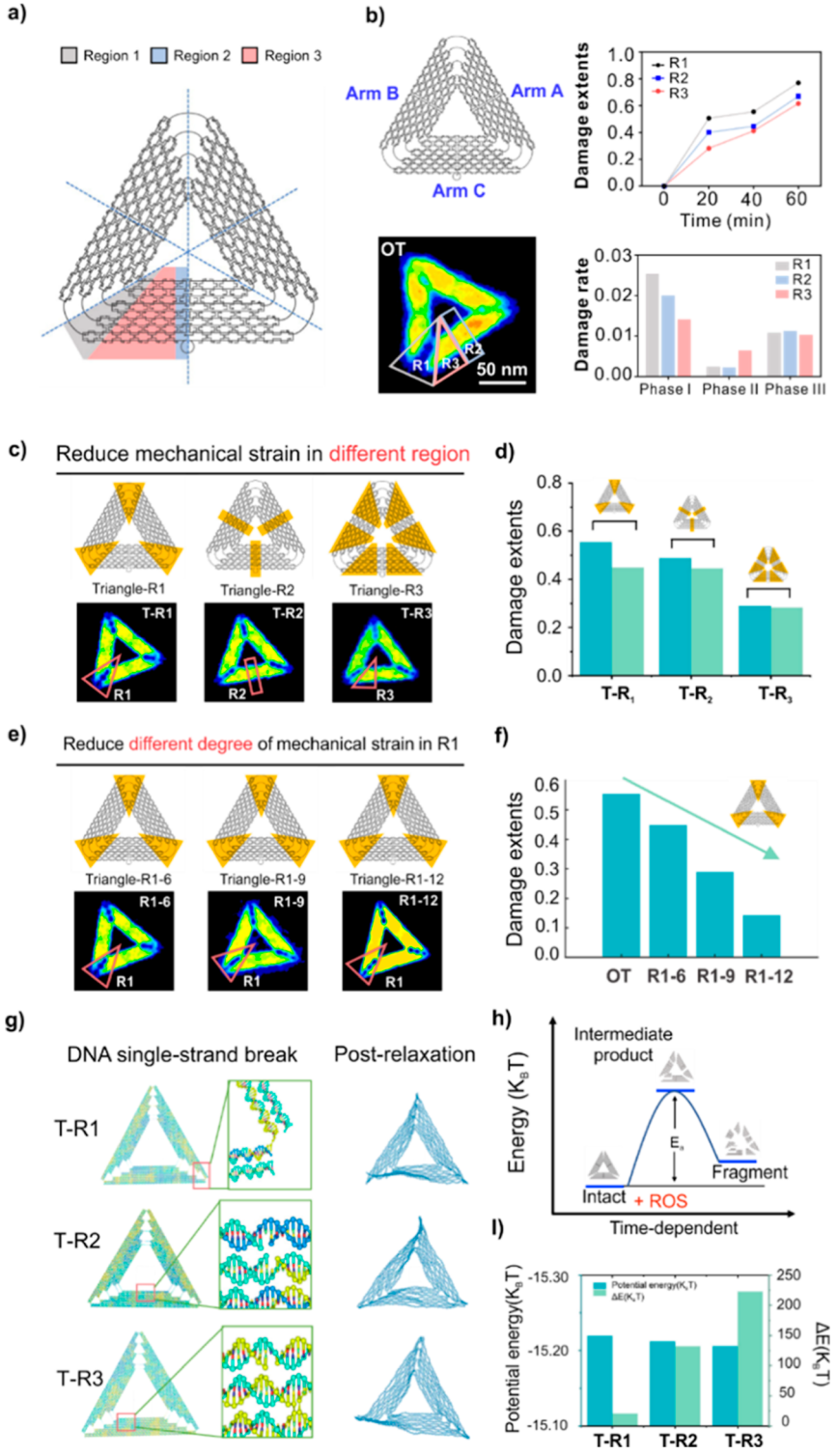

Figure 3. Mechanical stress-dependent ROS damage for higher-ordered DFNs. (a) Subregion division in triangular DFNs. (b) SPA processing of original triangular DFN after 20 min reaction with $^{\bullet}$OH. (c) SPA images of R1, R2, and R3 regions after reducing mechanical strain. (d) Damage extents of R1, R2, and R3 regions after reducing mechanical strain. (e) SPA images of R1 region after reducing different degrees of mechanical stress by removing 6, 9, and 12 staple strands. (f) Damage extents of R1 after reducing different degrees of mechanical stress by removing 6, 9, and 12 staple strands. (g–i) Theoretical calculations of the free energies of the triangular DFN and their corresponding intermediates based on DNA molecular dynamics (MD) simulation.

DFNs to interrogate the differences in reaction activity caused by intrinsic topological structures.

Geometrically, the connections between different subregions within the triangular DFNs generated mechanical stress naturally due to the folding pathway and bending degree of long DNA chains. Due to the strict C_3 symmetry of the triangular DFNs, the entire triangular structure could be segmented into six geometrically identical regions (Figure 3a). Hence, one

https://doi.org/10.1021/jacsau.4c01203
JACS Au 2025, 5, 965−974

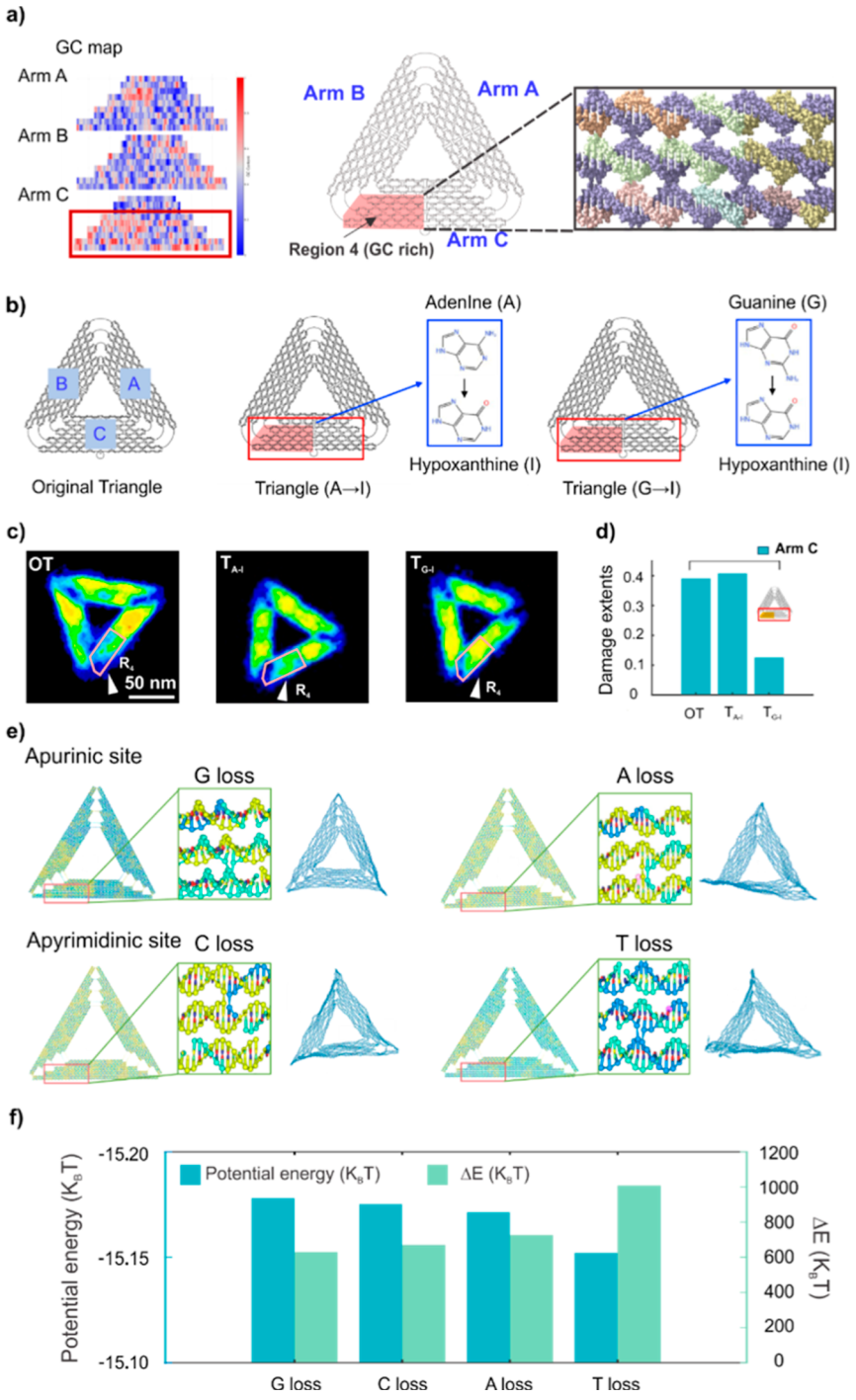

Figure 4. DNA base distribution-dependent ROS damage for higher-ordered DFNs. (a) R4 region: GC-rich trapezoidal region of the C arm. (b) Base-replacement experiment in R4 region, where I base was used to replace G and A bases. (c) SPA images of R4 after base replacement. (d) Damage extent of R4 after base replacement. (e,f) Theoretical calculations of the free energies of triangular DFNs and their corresponding intermediates based on DNA MD simulation.

region was chosen from the six and further divided into three individual subregions according to the distinct folding pathway of the long-chain DNA: region R1, where scaffold DNA rotated between adjacent arms; region R2, where scaffold DNA rotated within one arm; and region R3, where scaffold DNA stacked with each other within one arm.

Subsequently, we collected the AFM images of the R1, R2, and R3 regions post-reaction at 20, 40, and 60 min (Figure S16), statistically analyzed the dynamic changes via SPA for three regions, and plotted damage extents and damage rates, respectively, as shown in Figure 3b. We found that in phase I (0−20 min), the reaction rate in R1 was much faster than that in R2, which was also faster than that in R3. While in phase II (20−40 min), reaction rates in R3 become much faster; and in phase III (40−60 min), the reaction rates for the three regions had no significant difference. This result demonstrated that reactions in R1 and R2 regions possess higher reaction priority over R3, which was highly related with their geometry.

https://doi.org/10.1021/jacsau.4c01203
JACS Au 2025, 5, 965−974

Therefore, we speculate that this priority difference should be related to the fact that R1 and R2 are the bending regions during DNA folding in higher-ordered DFNs.[39,40] During the formation of DFNs, the DNA double helix folded or bent with a higher frequency and in a stiffer manner in the R1 and R2 regions, which generated higher mechanical stress correspondingly. For instance, the R1 area was the region where DNA strands connected and turned between adjacent arms, R2 was the region where long-chain DNA turned and folded within a single arm, and in contrast, R3 was the region where DNA double helices were parallelly stacked on the same plane without accumulating more mechanical stress. Hence, we concluded that regions with higher mechanical stress were more susceptible to ROS attack reactions.[41,42]

To validate this hypothesis, we removed 6 assembled single strands from R1, R2, and R3 regions of the DFNs, to reduce the mechanical stress in the corresponding areas, and then tested the difference in the ROS reaction in these areas before and after the removal via SPA (Figure 3c). By comparing the AFM images before and after removal, we found that the extent of damage in all three regions became smaller after reducing mechanical stress when reacting with •OH for 20 min, indicating that higher mechanical stress led to increased reactivity. More importantly, by comparing the extent of damage in three different regions before and after reducing mechanical stress, we found that the R1 region showed the highest reduction in average damage (19.1%), followed by R2 region (8.8%), with the R3 region showing the smallest reduction (2.8%) (Figure 3d). This damaged extent variation further indicated that different regions of the DFNs maintained different levels of mechanical stress, which were caused by the variations in DNA topological structures. When removing the same number of assembled single strands from the R1 region possessing the highest mechanical stress, the decreased ratio of mechanical stress was also the highest, which made the reaction less active, leading to the highest damage decrease. This was consistent with our previous speculation that regions with higher mechanical stress were more susceptible to ROS attack reactions. In other words, the more fragile the topologically region, the higher the mechanical stress and the faster the reaction rate will be.

After having tested the mechanical stress effect in different regions, we conducted a titration analysis of the mechanical stress release experiment in one specific region by removing 6, 9, and 12 assembled single strands from R1 to reduce different levels of stress (Figure 3e) and then compared the damage extents to further investigate the mechanical stress effect. Hence, we statistically analyzed the AFM images via the SPA method before and after the removals, and we found that the damage rates for R1−6, R1−9, and R1−12 were 44.8, 28.9, and 14.3%, respectively (Figure 3f). This meant the more strands we removed, the more the mechanical stress of the structure decreased, resulting in a corresponding decrease in the damage rate, which once again demonstrated that the higher the mechanical stress was, the higher the severity of the damage reaction caused.

Ultimately, we studied the impact of mechanical stress on ROS damage to DNA higher-order assembly structures through theoretical simulation. We used the DNA MD simulation software oxDNA to construct coarse-grained models of intermediates[43−45] (corresponding to different mechanical stress regions where chain breaks occurred for R1, R2, and R3 in the figure) (Figure 3g), and then calculated their free energies (detailed in the Supporting Information, Methods). The theoretical calculations of the free energies of triangle DFN and their corresponding intermediates indicated that intact triangle DFN exhibited the lowest energy level due to its stable structure, while the free energy of the corresponding intermediates was higher. This implied that the formation of intermediates through oxidative damage reactions had an energy barrier to cross over, which was provided by the chemical energy from ROS. The energy level of the intermediates corresponded to the reaction rates between triangle DFNs and ROS, where lower energy indicated a smaller energy barrier to be crossed, leading to a faster reaction rate. The entire process is a result of kinetic trapping (Figure 3h). From the simulation data, it can be observed that the product with chain breakage in the R1 region had the lowest energy, while the product in R3 had the highest energy. Therefore, the intermediate products with chain breakage in the R1 region with the lowest energy barrier (20.5 K_BT) compared with the reactants, were most likely to form. While the product in the R2 region (131.7 K_BT) and the R3 region (222.4 K_BT) required more energy. Hence, the intermediate structure was time-dependent due to this kinetic trapping (Figure 3i). These results further elucidated that mechanical stress within the DFNs was a key factor influencing its reaction rates and reaction sites with the ROS.

DNA Base Distribution-Dependent ROS Damage for Higher-Ordered DFNs

DNA double helix bundles, as the basic units that constituted the different shapes of DNA higher-order structures, were formed on their parallel stacking. This stacking method was identical across different higher-order structures in terms of configuration, with the only difference being the nucleotide-location of multiple DNA double helices (superhelices). Therefore, we further conducted a systematic study on the impact of DNA nucleotide distribution on ROS damage.

We first investigated the nucleotide-distribution effect on three different arms (arm A, B, and C). After a 40 min reaction with •OH, we found that C arm suffered more damage than the A and B arms (Figure S15), where the damage ratio of C arm was 45.3%, which was much higher than A and B arms (31.7 and 40.4%). Since the GC content in the C arm was much higher than the other two based on the GC content map shown in Figure 4a. In addition, there are differences in CG maps between DFNs (Figures S17−S20), and we believe this difference in damage extent was caused by the GC base distribution among different arms.

It was reported that purine base guanine (G) was the most easily oxidized one among the four bases, with its C8 position being the most prone to oxidation.[46−48] Under the action of strong oxidative free radicals, the G base tended to lose an electron, forming subsequent damage products such as 8-oxo-G, which in turn broke the DNA double helix state and displayed the imaging defects in AFM output. Therefore, we hypothesize that the preferential reaction sites of ROS in DFNs were distributed, not only in the regions with high mechanical stress but also in the regions with high G ratios.

To verify this hypothesis, we designated the GC-rich trapezoidal region in the C arm as R4 and conducted ROS damage research on it (Figure 4a). We conducted a base-replacement experiment in the R4 region. First, we introduced a new base (hypoxanthine, I)[49,50] to replace the residual bases. Since I base can hybridize with A, T, C, and G bases, it can still maintain the DNA superhelix structure after the replacement.[6,51−53] Subsequently, we conducted SPA processing

https://doi.org/10.1021/jacsau.4c01203
JACS Au 2025, 5, 965−974

before and after damage for three different groups: group 1 with the original R4 region, group 2 where I replaced all G bases in R4, and group 3 where I replaced all A bases in R4 (Figure 4b). After reacting with •OH for 40 min (Figure 4c), we found that compared to group 1, the damage extent of arm C in group 2 had a slightly increase from 39.1 to 40.9%, which meant I base was more reactive than A base with ROS. Meanwhile, the damage extent of arm C in group 3 decreased to 12.5%, showing that G base was more reactive than I base with ROS and the replacement of G base with I base could increase their resistance to ROS damage reaction. Hence, from the damage extent data shown in Figure 4d, we could conclude that the active reactivity of G base with ROS was greater than that of I base and then A base.

We then conducted theoretical simulations to further study the influence of DNA base-distribution on damage to high-level DNA structures. Using the DNA MD simulation software oxDNA,[43−45] we constructed coarse-grained models of intermediate products (lacking bases in R4 region) and generated products lacking guanine (G base missing), adenine (A base missing), thymine (T base missing), and cytosine (C base missing) sites. Subsequently, we calculated the free energy of four intermediates (detailed in Supporting Information, Methods) (Figure 4e,f). Theoretical calculations of the free energy of the intermediates corresponding to base damage in R4 region of triangle DFNs showed that the product with the missing G base had lower energy (639.3 K_BT) than the other three bases (670.2 K_BT for C base, 725.8 K_BT for A base, and 1008.2 K_BT for T base), making it the easiest to form, which was consistent with our previous experimental results. Furthermore, since this intermediate was structure-captured kinetically, its formation was also time-dependent. These results further elucidated that DNA base distribution inside higher-order DNA nanostructures was another key factor influencing the reaction rates and sites with ROS.

Reaction Energy Barrier Diagram for the Multistep Chemical Reactions Involved in ROS Damage on DFNs

Our results have demonstrated that there are two main factors determining the intermediate structure of the oxidative damage reaction in higher-order DNA nanostructures:

1 Mechanical stress: the reaction preferentially occurs at topologically fragile regions where the higher-ordered DNA nanostructures showing configurations with more bending and folding. These regions have higher mechanical stress and smaller steric hindrance, making themselves more susceptible for attack of ROS.
2 Nucleotide distribution: the ROS damage reaction is highly related to DNA bases of the DNA higher-ordered DNA assembly with diverse base distribution. The positions with high G base are more prone to react, compared with A, T, and C bases.

Therefore, based on experimental and theoretical simulation results, we have plotted the reaction energy barrier diagram for the entire ROS damage reaction of DFN in Figure 5. We found that this reaction followed a kinetically trapped process.[41] First, the earliest intermediates formed were the mechanically stress-dominated products, which corresponded to three types of products: the product with chain breakage in R1 (20.5 K_BT), the product with chain breakage in R2 (131.7 K_BT), and the product with chain breakage in R3 (222.4 K_BT). Lower energy values indicated easier product formation and shorter half-lives (15.7, 23.4, and 26.8 min for R1, R2, and R3). The subsequent

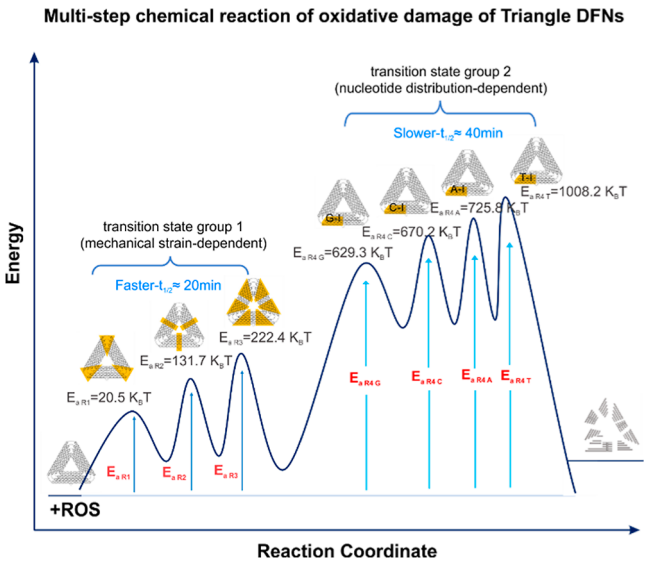

Figure 5. Reaction energy barrier diagram for the multistep chemical reactions involved in ROS damage on DFNs.

products were predominantly influenced by the base distribution, which was mainly related to the GC distribution inside the higher-ordered DFNs. This group corresponded to four base-oxidized products: G, C, A, and T base-oxidation products. The activation energy for the formation of the G base-oxidation product was 629.3 K_BT, the lowest among the four bases, making it the most easily formed product in the nucleotide distribution-dependent group. Meanwhile, the activation energy for C, A, and T base oxidation were 670.2, 725.8, and 1008.2 K_BT, respectively. The half-life for the R4 region was 41.2 min, which was almost twice that for the reactions occurring in the R1−R3 regions. Hence, the reaction process between ROS and DFN could be illustrated, showing the different intermediates along the direction of the reaction.

CONCLUSIONS

In summary, we have developed a new SPA method based on the reconstruction and reprocessing of AFM images to visualize the process of damage of ROS to higher-order DNA structures simulated by DFNs. This new SPA method allows for localization of molecular reaction regions in real-time while ensuring resolution, which can track the dynamic changes, reaction sites, and regions of DFNs during the reaction process. Using this method, we have found that the kinetics of the reaction between DNA nanostructures and ROS is highly dependent on their topologies, where local mechanical stress and regional base distribution greatly affect the reaction activation energy. These findings provide new research tools and perspectives for studying the ROS damage of highly folded and stacked DNA structural domains and help reveal the key mechanisms behind their functional differences in topologically associating domains.

MATERIALS AND METHODS

Reagents

All DNA staple strands were purchased from Sangon (Shanghai, China) and were used as received. M13mp18 single-stranded DNA (7249) was purchased from New England Biolabs. P7560 was purchased from Tilibit (Munich, Germany). Gelred, agarose, and a gel loading buffer

https://doi.org/10.1021/jacsau.4c01203
JACS Au 2025, 5, 965−974

were purchased from BioRad. All other chemicals were purchased from Sigma-Aldrich.

Synthesis of DNA Origami Nanostructures

Triangle, rectangle, cross, and hexagon were synthesized in this work, and the structure design and annealing procedures were based on previously reported methods. The scaffold strand of all of the DNA origami was M13mp18, except for hexagon, whose scaffold strand was p7560. The scaffold strands (400 nM, 5 μL), 5-fold excess staple strands (500 nM, 20 μL), folding buffer (10 μL), and ddH_2O (65 μL) were added to a 100 μL PCR tube and annealed in PCR. Triangle, rectangle, and cross were annealed in 1 × TAE/Mg^{2+} buffer (40 mM Tris, 2 mM EDTA, and 12.5 mM magnesium acetate, pH 8.0) using the reported annealing procedure. Hexagon was annealed in folding buffer (5 mM Tris base, 1 mM EDTA, and 14 mM $MgCl_2$, pH 8.0) using the reported procedure (65 °C for 5 min, 60 to 24 °C, at 120 min/°C). After annealing, the synthesized DNA origami is ultrafiltered 3−4 times at 3500 g for 5 min in a 100 KD ultrafiltration tube to remove the free staple strands. The purified samples are quantified using Nanodrop.

Oxidative Damage of DNA Origami in the Presence of PCN Nanomaterials

DNA origami (50 nM, 200 μL) and PCN (1 g/L, 200 μL) were mixed in a beaker with a final volume of 2 mL. To ensure that only $^{\bullet}OH$ is generated in the solution, catalase (4000 units/mL, 100 μL) was added to the solution to remove the additional H_2O_2 produced by PCN. Then, the beaker was placed under a xenon lamp equipped with ultraviolet reflector and band-pass filter (365 nm) for illumination (10 mW/cm^2), and the solution (100 μL) was collected at different time points. To avoid the interference of PCN with DNA origami during AFM imaging, the sample solution was centrifuged at 6000 rpm for 2 min to allow PCN to form a precipitate, and the supernatant after centrifugation was taken and reserved for subsequent imaging.

AFM Characterization and Analysis

The morphological changes of DNA origami after oxidative damage at different times and under different reaction conditions were characterized by AFM (Multimode Nanoscope VIII, Bruker). All samples (2 nM, 10 μL) were dripped onto a freshly peeled mica surface and incubated at room temperature for 5 min. The sample was scanned with SCANASYST-FLUID+ tips (Bruker) and conducted under a PeakForce QNM in Fluid imaging mode. The scan size was 2 μm, and representative fields of view were selected for characterization, 2−3 parallel samples were taken for each condition, and at least 5 images were taken for each sample. The representative images were then processed using NanoScope Analysis 2.0 (Bruker).

Statistical Distributions of the Relative Area of the Prepared DNA Origami

ImageJ was used to quantify the average origami area at each time point, which was regarded as the residual concentration of reactants at the current time point (C_t), while the intact DNA origami area was regarded as the initial concentration of the reaction (C_0), and C_t/C_0 was used to represent the degree of damage. Through the curve fitting of the results, we found that the reaction kinetic process of ROS and DNA origami was in line with the first-order kinetic reaction; that is, $\ln(C_t/C_0)$ was linearly correlated with the reaction time. The kinetic equations of four reactions were obtained, and the slope in the equation was the kinetic constant (k) of the reaction.

SPA of DNA Origami AFM Images

Step 1: NanoScope Analysis 2.0 software was used to preprocess the .spm format file. In Choose Color Table, select Gray Colormap, and in Modify Data Scale, adjust the Contrast display range, with Minimum slightly less than the lower limit of the data range and Maximum slightly greater than the upper limit of the data range, and round up to the nearest whole number. Check Use linear interpolation. Export as a TIFF image, note that the dpi is set to 600, the image width is 4.4 in., and the height is 3.6 in. And display the scale bar and color bar.

Step 2: manually labeling was performed using ImageJ software. Import the TIFF format image into ImageJ and use the Polygon selection tool to complete the labeling (single particle circling), and add the ROI Manager. After completing the initial circling of all the monolithic structures, choose to save it as RoiSet.zip and put it into a directory with the original image in TIFF format as a data package.

Step 3: the data packet is processed using a program that extracts the circle-selected individual particles and performs particle alignment (Particle alignment).

Step 4: the program will export the output compressed package after decompression, the entire folder into ImageJ, open for stack, select z-axis projection, and select average can be averaged particles. Subsequently, use LUT to select the pseudo color, and use analyze particles to calculate the resulting image area, the height of the statistical calculation.

Thermal GC Maps of the DNA Origami

Use DNA Origami Visualization Tools to draw the GC maps of five types of DNA origami with different morphologies, input the CaDNAno json file of DNA origami and the corresponding Scaffold length and Scaffold Sequence, and check Generate a heatmap of GC content to get the thermal GC map corresponding to the DNA origami.

Coarse-grained modeling and calculation of DNA origami: OxDNA-based simulations were conducted to enhance the comprehension of the energy landscape in the process of multistep chemical reactions of oxidative damage of DNA higher-order structure. The oxDNA model is parametrized in a top-down manner, with each nucleotide represented as a site featuring six anisotropic interactions: excluded volume effects, stacking and cross-stacking forces, hydrogen bonding, backbone connectivity, and electrostatic repulsion. Here, we employed the refined oxDNA2 force field with explicit electrostatics.

We have engineered seven distinct structures representative of various forms of damage to function as the starting point for our molecular simulations. After the initial structures were set, they were subsequently relaxed in a two-step process. First, a Monte Carlo simulation was performed using the DNA_relax force fields. This was subsequently followed up with an additional relaxation achieved by utilizing the max_backbone_force option within a MD simulation under the DNA2 force field. The production simulations were performed in the canonical *NVT* ensemble at 300 K using an Anderson-like thermostat, The simulation time step for integration was 6.06 fs (0.002 oxDNA time units), MD steps were set 1×10^9 that was enough for each system to study the energy landscape, The particle translational diffusion coefficient was set to 2.5, which is about ∼2 orders of magnitude faster than in the experiment to accelerate diffusive dynamics and improve sampling. The Newtonian step of an Anderson-like thermostat was 103. And configurations were saved for analysis every 1×10^4 steps. The salt condition for all simulations was set to a monovalent NaCl concentration of 1 M NaCl. In the MD simulations, the potential energy of different structures was recorded in the energy file every 2×10^4 steps. The mean energy of each structure was derived by averaging the last 2000 sample points (50,000 energy points in total) when the simulation reached equilibrium. The DNA structure configurations were derived from the trajectory file and were exported into high-quality images using oxView.

■ ASSOCIATED CONTENT

Supporting Information

The Supporting Information is available free of charge at https://pubs.acs.org/doi/10.1021/jacsau.4c01203.

Materials and reagents, synthesis of DNA origami nanostructures, oxidative damage of DNA origami in the presence of PCN nanomaterials, AFM characterization and analysis, statistical distributions of the relative area of the prepared DNA origami, SPA of DNA origami AFM images, and coarse-grained modeling and calculation of DNA origami (PDF)

https://doi.org/10.1021/jacsau.4c01203
JACS Au 2025, 5, 965−974

AUTHOR INFORMATION

Corresponding Authors

Mingqiang Li − *School of Chemistry and Chemical Engineering, New Cornerstone Science Laboratory, Frontiers Science Center for Transformative Molecules, Zhangjiang Institute for Advanced Study and National Center for Translational Medicine, Shanghai Jiao Tong University, Shanghai 200240, China;* orcid.org/0000-0001-9854-2251; Email: limingqiang@sjtu.edu.cn

Zhilei Ge − *School of Chemistry and Chemical Engineering, New Cornerstone Science Laboratory, Frontiers Science Center for Transformative Molecules, Zhangjiang Institute for Advanced Study and National Center for Translational Medicine, Shanghai Jiao Tong University, Shanghai 200240, China;* orcid.org/0000-0001-7184-7565; Email: gezhilei@sjtu.edu.cn

Authors

Shuangye Zhang − *School of Chemistry and Chemical Engineering, New Cornerstone Science Laboratory, Frontiers Science Center for Transformative Molecules, Zhangjiang Institute for Advanced Study and National Center for Translational Medicine, Shanghai Jiao Tong University, Shanghai 200240, China*

Xiaodong Xie − *School of Chemistry and Chemical Engineering, New Cornerstone Science Laboratory, Frontiers Science Center for Transformative Molecules, Zhangjiang Institute for Advanced Study and National Center for Translational Medicine, Shanghai Jiao Tong University, Shanghai 200240, China*

Hairuo Zhang − *School of Chemistry and Chemical Engineering, New Cornerstone Science Laboratory, Frontiers Science Center for Transformative Molecules, Zhangjiang Institute for Advanced Study and National Center for Translational Medicine, Shanghai Jiao Tong University, Shanghai 200240, China*

Ziwei Zhao − *Shanghai Artificial Intelligence Research Institute, Shanghai 200240, China*

Kai Xia − *Shanghai Artificial Intelligence Research Institute, Shanghai 200240, China*

Haitao Song − *Shanghai Artificial Intelligence Research Institute, Shanghai 200240, China;* orcid.org/0000-0003-2113-2224

Qian Li − *School of Chemistry and Chemical Engineering, New Cornerstone Science Laboratory, Frontiers Science Center for Transformative Molecules, Zhangjiang Institute for Advanced Study and National Center for Translational Medicine, Shanghai Jiao Tong University, Shanghai 200240, China*

Complete contact information is available at: https://pubs.acs.org/10.1021/jacsau.4c01203

Author Contributions

§S.Z. and X.X. contributed equally to this work.

Funding

This work was supported by the National Natural Science Foundation of China (23Z031503509, 21991134, and T2188102), the New Cornerstone Science Foundation, and the 2022 Shanghai "Science and Technology Innovation Action Plan" Fundamental Research Project (22JC1401202).

Notes

The authors declare no competing financial interest.

REFERENCES

(1) Watson, J.; Crick, F. Molecular Structure of Nucleic Acids - a Structure for Deoxyribose Nucleic Acid. *Nature* **1953**, *171* (4356), 737−738.

(2) Luger, K.; Mader, A.; Richmond, R.; Sargent, D.; Richmond, T. Crystal Structure of the Nucleosome Core Particle at 2.8 Angstrom Resolution. *Nature* **1997**, *389* (6648), 251−260.

(3) Kanvah, S.; Joseph, J.; Schuster, G.; Barnett, R.; Cleveland, C.; Landman, U. Oxidation of DNA: Damage to Nucleobases. *Acc. Chem. Res.* **2010**, *43* (2), 280−287.

(4) Arnould, C.; Rocher, V.; Saur, F.; Bader, A.; Muzzopappa, F.; Collins, S.; Lesage, E.; Le Bozec, B.; Puget, N.; Clouaire, T.; Mangeat, T.; Mourad, R.; Ahituv, N.; Noordermeer, D.; Erdel, F.; Bushell, M.; Marnef, A.; Legube, G. Chromatin Compartmentalization Regulates the Response to DNA Damage. *Nature* **2023**, *623* (7985), 183−192.

(5) Papamichos-Chronakis, M.; Peterson, C. Chromatin and the Genome Integrity Network. *Nat. Rev. Genet.* **2013**, *14* (1), 62−75.

(6) Lindahl, T. Instability and Decay of the Primary Structure of DNA. *Nature* **1993**, *362* (6422), 709−715.

(7) Sancar, A.; Lindsey-Boltz, L.; Ünsal-Kaçmaz, K.; Linn, S. Molecular Mechanisms of Mammalian DNA Repair and the DNA Damage Checkpoints. *Annu. Rev. Biochem.* **2004**, *73*, 39−85.

(8) Negrini, S.; Gorgoulis, V.; Halazonetis, T. Genomic Instability - an Evolving Hallmark of Cancer. *Nat. Rev. Mol. Cell Biol.* **2010**, *11* (3), 220−228.

(9) Ochs, F.; Karemore, G.; Miron, E.; Brown, J.; Sedlackova, H.; Rask, M.; Lampe, M.; Buckle, V.; Schermelleh, L.; Lukas, J.; Lukas, C. Stabilization of Chromatin Topology Safeguards Genome Integrity. *Nature* **2019**, *574* (7779), 571−574.

(10) Kruhlak, M.; Celeste, A.; Dellaire, G.; Fernandez-Capetillo, O.; Müller, W.; McNally, J.; Bazett-Jones, D.; Nussenzweig, A. Changes in Chromatin Structure and Mobility in Living Cells at Sites of DNA Double-Strand Breaks. *J. Cell Biol.* **2006**, *172* (6), 823−834.

(11) Fortuny, A.; Chansard, A.; Caron, P.; Chevallier, O.; Leroy, O.; Renaud, O.; Polo, S. Imaging the Response to DNA Damage in Heterochromatin Domains Reveals Core Principles of Heterochromatin Maintenance. *Nat. Commun.* **2021**, *12* (1), 2428.

(12) Fang, W.; Xie, M.; Hou, X.; Liu, X.; Zuo, X.; Chao, J.; Wang, L.; Fan, C.; Liu, H.; Wang, L. DNA Origami Radiometers for Measuring Ultraviolet Exposure. *J. Am. Chem. Soc.* **2020**, *142* (19), 8782−8789.

(13) Song, J.; Arbona, J.-M.; Zhang, Z.; Liu, L.; Xie, E.; Elezgaray, J.; Aime, J.-P.; Gothelf, K.; Besenbacher, F.; Dong, M. Direct Visualization of Transient Thermal Response of a DNA Origami. *J. Am. Chem. Soc.* **2012**, *134* (24), 9844−9847.

(14) Lei, Y.; Li, C.; Ji, X.; Sun, H.; Liu, X.; Mao, Z.; Chen, W.; Qing, Z.; Liu, J. Lowering Entropic Barriers in Triplex DNA Switches Facilitating Biomedical Applications at Physiological Ph. *Angew. Chem., Int. Ed.* **2024**, *63* (19), No. e202402123.

(15) Gu, L.; Ding, Y.; Zhou, Y.; Zhang, Y.; Wang, D.; Liu, J. Selective Hemin Binding by a Non-G-Quadruplex Aptamer with Higher Affinity and Better Peroxidase-Like Activity. *Angew. Chem., Int. Ed.* **2024**, *63* (6), No. e202314450.

(16) Chen, J.; Gu, P.; Ran, G.; Zhang, Y.; Li, M.; Chen, B.; Lu, H.; Han, Y.-Z.; Zhang, W.; Tang, Z.; Yan, Q.; Sun, R.; Fu, X.; Chen, G.; Shi, Z.; Wang, S.; Liu, X.; Li, J.; Wang, L.; Zhu, Y.; Shen, J.; Tang, B.; Fan, C. Atomically Precise Photothermal Nanomachines. *Nat. Mater.* **2024**, *23* (2), 271−280.

(17) Dey, S.; Fan, C.; Gothelf, K.; Li, J.; Lin, C.; Liu, L.; Liu, N.; Nijenhuis, M.; Saccà, B.; Simmel, F.; Yan, H.; Zhan, P. DNA Origami. *Nat. Rev. Methods Primers* **2021**, *1* (1), 13.

(18) Ge, Z.; Gu, H.; Li, Q.; Fan, C. Concept and Development of Framework Nucleic Acids. *J. Am. Chem. Soc.* **2018**, *140* (51), 17808−17819.

(19) Seo, J.; Kim, S.; Park, H.; Choi, D.; Nam, J. Nano-Bio-Computing Lipid Nanotablet. *Sci. Adv.* **2019**, *5* (2), No. eaau2124.

(20) Liu, L.; Hong, F.; Liu, H.; Zhou, X.; Jiang, S.; Sulc, P.; Jiang, J.; Yan, H. A Localized DNA Finite-State Machine with Temporal Resolution. *Sci. Adv.* **2022**, *8* (12), No. eabm9530.

(21) Kim, Y.; Nam, J. Mechanically Interlocked Gold Nanocatenanes. *Nat. Synth.* **2022**, *1* (8), 649−657.
(22) Zhou, B.; Yang, B.; Liu, Q.; Jin, L.; Shao, Y.; Yuan, T.; Zhang, Y.; Wang, C.; Shi, Z.; Li, X.; Pan, Y.; Qiao, N.; Xu, J. F.; Yang, Y.; Dong, Y.; Xu, L.; Gui, S.; Liu, D. Effects of Univariate Stiffness and Degradation of DNA Hydrogels on the Transcriptomics of Neural Progenitor Cells. *J. Am. Chem. Soc.* **2023**, *145* (16), 8954−8964.
(23) Yu, L.; Xu, Y.; Al-Amin, M.; Jiang, S.; Sample, M.; Prasad, A.; Stephanopoulos, N.; Sulc, P.; Yan, H. Cytodirect: A Nucleic Acid Nanodevice for Specific and Efficient Delivery of Functional Payloads to the Cytoplasm. *J. Am. Chem. Soc.* **2023**, *145* (50), 27336−27347.
(24) Li, X.; Dai, X.; Pan, Y.; Sun, Y.; Yang, B.; Chen, K.; Wang, Y.; Xu, J.-F.; Dong, Y.; Yang, Y.; Yan, L.-T.; Liu, D. Studies on the Synergistic Effect of Tandem Semi-Stable Complementary Domains on Sequence-Defined DNA Block Copolymers. *J. Am. Chem. Soc.* **2022**, *144* (46), 21267−21277.
(25) Zhou, X.; Satyabola, D.; Liu, H.; Jiang, S.; Qi, X.; Yu, L.; Lin, S.; Liu, Y.; Woodbury, N.; Yan, H. Two-Dimensional Excitonic Networks Directed by DNA Templates as an Efficient Model Light-Harvesting and Energy Transfer System. *Angew. Chem., Int. Ed.* **2022**, *61* (51), No. e2022112.
(26) Heng, H.; Song, G.; Cai, X.; Sun, J.; Du, K.; Zhang, X.; Wang, X.; Feng, F.; Wang, S. Intrinsic Mitochondrial Reactive Oxygen Species (Ros) Activate the in Situ Synthesis of Trimethine Cyanines in Cancer Cells. *Angew. Chem., Int. Ed.* **2022**, *61* (38), No. e202203444.
(27) Yin, F.; Li, M.; Mao, X.; Li, F.; Xiang, X.; Li, Q.; Wang, L.; Zuo, X.; Fan, C.; Zhu, Y. DNA Framework-Based Topological Cell Sorters. *Angew. Chem., Int. Ed.* **2020**, *59* (26), 10406−10410.
(28) Scheckenbach, M.; Schubert, T.; Forthmann, C.; Glembockyte, V.; Tinnefeld, P. Self-Regeneration and Self-Healing in DNA Origami Nanostructures. *Angew. Chem., Int. Ed.* **2021**, *60* (9), 4931−4938.
(29) Cheng, Y.; Grigorieff, N.; Penczek, P.; Walz, T. A Primer to Single-Particle Cryo-Electron Microscopy. *Cell* **2015**, *161* (3), 438−449.
(30) Beagan, J.; Phillips-Cremins, J. On the Existence and Functionality of Topologically Associating Domains. *Nat. Genet.* **2020**, *52* (1), 8−16.
(31) Szabo, Q.; Bantignies, F.; Cavalli, G. Principles of Genome Folding into Topologically Associating Domains. *Sci. Adv.* **2019**, *5* (4), No. eaaw1668.
(32) Felsenfeld, G.; Groudine, M. Controlling the Double Helix. *Nature* **2003**, *421* (6921), 448−453.
(33) Luger, K.; Dechassa, M.; Tremethick, D. New Insights into Nucleosome and Chromatin Structure: An Ordered State or a Disordered Affair? *Nat. Rev. Mol. Cell Biol.* **2012**, *13* (7), 436−447.
(34) Rothemund, P. Folding DNA to Create Nanoscale Shapes and Patterns. *Nature* **2006**, *440* (7082), 297−302.
(35) Wang, P.; Gaitanaros, S.; Lee, S.; Bathe, M.; Shih, W.; Ke, Y. Programming Self-Assembly of DNA Origami Honeycomb Two-Dimensional Lattices and Plasmonic Metamaterials. *J. Am. Chem. Soc.* **2016**, *138* (24), 7733−7740.
(36) Suzuki, Y.; Endo, M.; Sugiyama, H. Lipid-Bilayer-Assisted Two-Dimensional Self-Assembly of DNA Origami Nanostructures. *Nat. Commun.* **2015**, *6*, 8052.
(37) Pang, J.; Aquino, K.; Oldehinkel, M.; Robinson, P.; Fulcher, B.; Breakspear, M.; Fornito, A. Geometric Constraints on Human Brain Function. *Nature* **2023**, *618* (7965), 566−574.
(38) Chen, D.; Liu, J.; Wu, J.; Wei, G.; Pan, F.; Yau, S. Path Topology in Molecular and Materials Sciences. *J. Phys. Chem. Lett.* **2023**, *14* (4), 954−964.
(39) Ji, J.; Karna, D.; Mao, H. DNA Origami Nano-Mechanics. *Chem. Soc. Rev.* **2021**, *50* (21), 11966−11978.
(40) Chen, H.; Weng, T.-W.; Riccitelli, M.; Cui, Y.; Irudayaraj, J.; Choi, J. Understanding the Mechanical Properties of DNA Origami Tiles and Controlling the Kinetics of Their Folding and Unfolding Reconfiguration. *J. Am. Chem. Soc.* **2014**, *136* (19), 6995−7005.
(41) Kosinski, R.; Mukhortava, A.; Pfeifer, W.; Candelli, A.; Rauch, P.; Saccà, B. Sites of High Local Frustration in DNA Origami. *Nat. Commun.* **2019**, *10* (1), 1061.
(42) Shrestha, P.; Emura, T.; Koirala, D.; Cui, Y.; Hidaka, K.; Maximuck, W.; Endo, M.; Sugiyama, H.; Mao, H. Mechanical Properties of DNA Origami Nanoassemblies Are Determined by Holliday Junction Mechanophores. *Nucleic Acids Res.* **2016**, *44* (14), 6574−6582.
(43) Wang, J.; Wei, Y.; Zhang, P.; Wang, Y.; Xia, Q.; Liu, X.; Luo, S.; Shi, J.; Hu, J.; Fan, C.; Li, B.; Wang, L.; Zhou, X.; Li, J. Probing Heterogeneous Folding Pathways of DNA Origami Self-Assembly at the Molecular Level with Atomic Force Microscopy. *Nano Lett.* **2022**, *22* (17), 7173−7179.
(44) Snodin, B.; Schreck, J.; Romano, F.; Louis, A.; Doye, J. Coarse-Grained Modelling of the Structural Properties of DNA Origami. *Nucleic Acids Res.* **2019**, *47* (3), 1585−1597.
(45) Snodin, B.; Romano, F.; Rovigatti, L.; Ouldridge, T.; Louis, A.; Doye, J. Direct Simulation of the Self-Assembly of a Small DNA Origami. *ACS Nano* **2016**, *10* (2), 1724−1737.
(46) Sugiyama, H.; Saito, I. Theoretical Studies of Gg-Specific Photocleavage of DNA Via Electron Transfer: Significant Lowering of Ionization Potential and 5'-Localization of Homo of Stacked Gg Bases in B-Form DNA. *J. Am. Chem. Soc.* **1996**, *118* (30), 7063−7068.
(47) Steenken, S.; Jovanovic, S. How Easily Oxidizable Is DNA? One-Electron Reduction Potentials of Adenosine and Guanosine Radicals in Aqueous Solution. *J. Am. Chem. Soc.* **1997**, *119* (3), 617−618.
(48) Li, H.; Endutkin, A.; Bergonzo, C.; Fu, L.; Grollman, A.; Zharkov, D.; Simmerling, C. DNA Deformation-Coupled Recognition of 8-Oxoguanine: Conformational Kinetic Gating in Human DNA Glycosylase. *J. Am. Chem. Soc.* **2017**, *139* (7), 2682−2692.
(49) Leonard, G.; Booth, E.; Hunter, W.; Brown, T. The Conformational Variability of an Adenosine Inosine Base-Pair in a Synthetic DNA Dodecamer. *Nucleic Acids Res.* **1992**, *20* (18), 4753−4759.
(50) Kawase, Y.; Iwai, S.; Inoue, H.; Miura, K.; Ohtsuka, E. Studies on Nucleic Acid Interactions I. Stabilities of Mini-Duplexes (Dg2a4xa4g2-Dc2t4yt4c2) and Self-Complementary D(Gggaaxyttccc) Containing Deoxyinosine and Other Mismatched Bases. *Nucleic Acids Res.* **1986**, *14* (19), 7727−7736.
(51) Copeland, W.; Lam, N.; Wang, T. Fidelity Studies of the Human DNA Polymerase-Alpha - the Most Conserved Region among Alpha-Like DNA-Polymerases Is Responsible for Metal-Induced Infidelity in DNA-Synthesis. *J. Biol. Chem.* **1993**, *268* (15), 11041−11049.
(52) Lindahl, T.; Nyberg, B. Rate of Depurination of Native Deoxyribonucleic Acid. *Biochemistry* **1972**, *11* (19), 3610−3618.
(53) Kunkel, T.; Bebenek, R. DNA Replication Fidelity. *Annu. Rev. Biochem.* **2000**, *69*, 497−529.

https://doi.org/10.1021/jacsau.4c01203
JACS Au 2025, 5, 965−974